Supporting Information

Reinforced gel-state polybenzimidazole hydrogen separators for alkaline water electrolysis

Muhammad Luthfi Akbar Trisno,[1,2] Asridin Dayan,[1,2] Su Ji Lee,[1] Franz Egert,[3] Martina Gerle,[3] Mikkel Rykær Kraglund,[4] Jens Oluf Jensen,[4] David Aili,[4] Aleksandra Roznowska,[5] Artur Michalak,[5*] Hyun S. Park,[1,2] Fatemeh Razmjooei,[3*] Syed-Asif Ansar,[3] Dirk Henkensmeier[1,2*]

1 Hydrogen · Fuel Cell Research Center, Korea Institute of Science and Technology (KIST), Seoul 02792, Republic of Korea.

2 Division of Energy & Environment Technology, KIST School, University of Science and Technology (UST), Seoul 02792, Republic of Korea.

3 Institute of Engineering Thermodynamics, German Aerospace Center (DLR), 70569 Stuttgart, Germany.

4 Department of Energy Conversion and Storage, Technical University of Denmark (DTU), Fysikvej 310, 2800 Kgs. Lyngby, Denmark.

5 Department of Theoretical Chemistry, Faculty of Chemistry, Jagiellonian University, 30-387 Krakow, Poland.

* corresponding authors: michalak@chemia.uj.edu.pl, Fatemeh.Razmjooei@dlr.de, henkensmeier@kist.re.kr

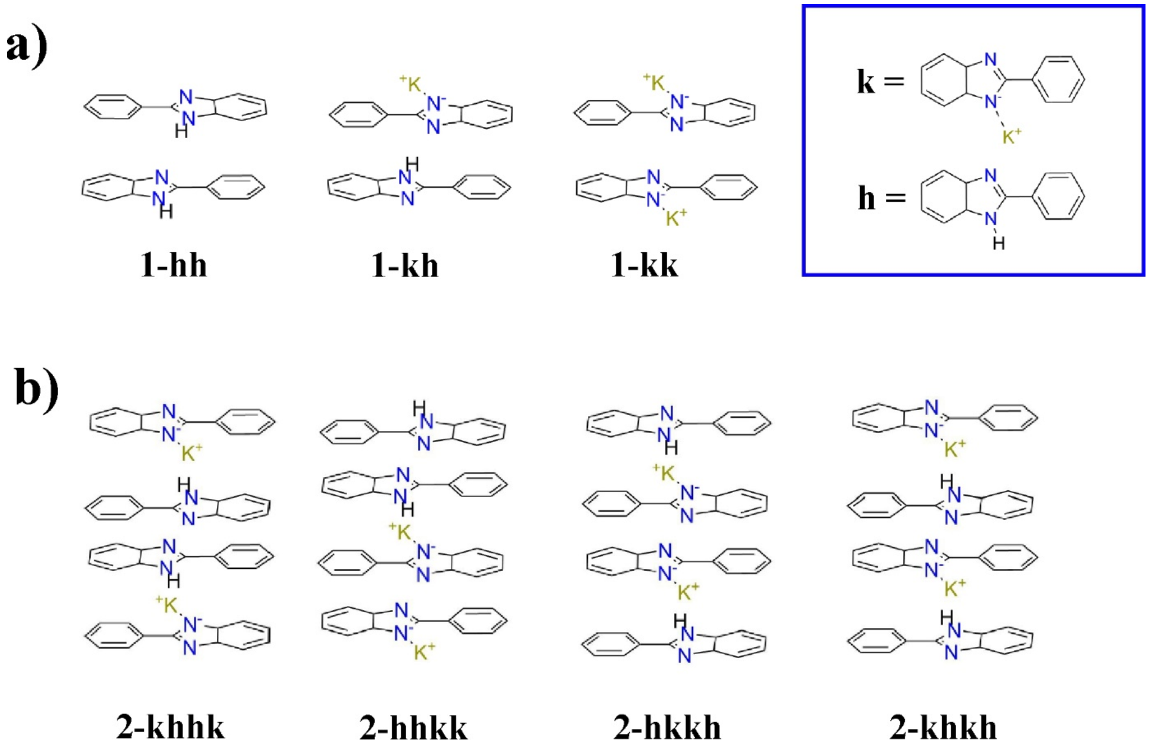

Figure S1: Considered models of systems containing two (part **a**) and four interacting units (part **b**). The **h**-fragment corresponds to 2-phenylbenzimidazole and the **k**-fragment to potassium 2-phenylbenzimidazolide.

Computational details

In theoretical part, Density Functional Theory (DFT) was used as primary method. In order to explore large variety of possible structures, a combined computational protocol was used, in which DFT geometry optimizations were performed for the geometries from semiempirical molecular dynamics (MD) trajectories or Monte-Carlo based structure-generation based approach. Similar approaches were used in our previous studies. [S1, S2] Semi-empirical calculations with PM7 [S3] method were performed using MOPAC 2016 program [S4]. DFT calculations were performed with the ADF program (v. 2019.304, 2020.103), [S5-S7] with BP86 functional [S8, S9], and Grimme D3 dispersion correction with Becke-Johnson damping, [S10] and the Slater-type all-electron TZP basis set [S11]. As in the previous applications, [S1, S2] locally developed programs were used for MD simulations and Monte-Carlo-based structure generation, utilizing PM7-determined forces/energies.

Construction of models

The model systems built of 2, 4, and 8 interacting units of 2-phenylbenzimidazole (**h** fragment), and potassium 2-phenylbenzimidazolide (**k** fragment) were systematically analyzed. The systems **1**, and **2** based on 2, and 4 units, respectively, are schematically depicted in **Figure S1**.

In the first step, a variety of structures for **1-hh**, **1-kh**, and **1-kk** models (**Figure S1a**) was optimized based on the structures generated from semiempirical (PM7) MD-trajectory (100 ps; 100,000 steps, time step - 1fs, T = 373K, 2 starting structures for each type of system); every 100th structure from MD trajectory was optimized first on the semiempirical-level, and then on the DFT-level. Obtained set of structures included structures with hydrogen bonding, as well as π-stacking interactions.

Two groups of structures were separately considered: those containing hydrogen-bonding, and those involving solely π-stacking interactions. The minimum-energy structures for **1-hh**, **1-kh**, and **1-kk,** from both aforementioned groups were further used to build the systems **2** with four **h/k** units (**Figure S1b**). The idea of constructing the systems **2**, is presented in **Figure S2.** Initial geometry for each of the system was constructed based on the lowest-energy structure of the corresponding **1**-system placed in the middle (frame in **Figure S2**), and adding two "outside" fragments. Here, the Monte-Carlo based approach was used for adding those two fragments, attached in the random position and orientation to the middle-core dimer; 1000 structures were generated for each of the system. In addition, some structures were constructed by adding the two "outside" units manually, to enforce the specific interactions. All the structures were optimized on the semi-empirical level. 10 lowest-energy-, and every 10th (in PM7 energy order) structure were optimized on the DFT-level.

Finally, the systems containing 8 units in total, were constructed in a similar way, by utilizing the minimum-energy structures for **2-khhk, 2-hhkk, 2-hkhk, 2-khkh,** combined with the minimum-energy structures obtained for respective **1-hh**, **1-kh**, and **1-kk** models.

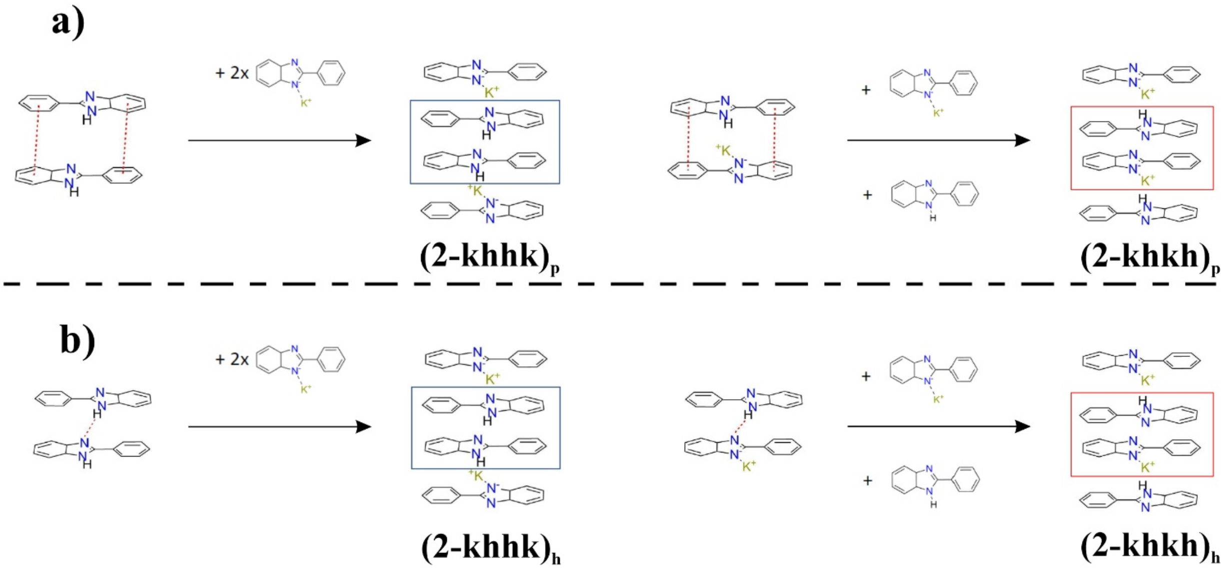

Figure S2: The idea of construction of **2** models based on minimum-energy **1**-structures in the case of: a) π-stacking interaction; b) hydrogen bonded groups of structures.

Results.

Examples of different types of structures for **1-hh**, **1-hk** and **1-kk** systems, together with the values of the shortest N-N distance, and relative energies are shown in **Figure S3**. The lowest energy structures of considered types of **2** models are shown in **Figure S4**. The results clearly indicate that the shortest N-N distances in the range of 2.7-2.9Å can be observed only in the structures in which N-H---N hydrogen bonding is present.

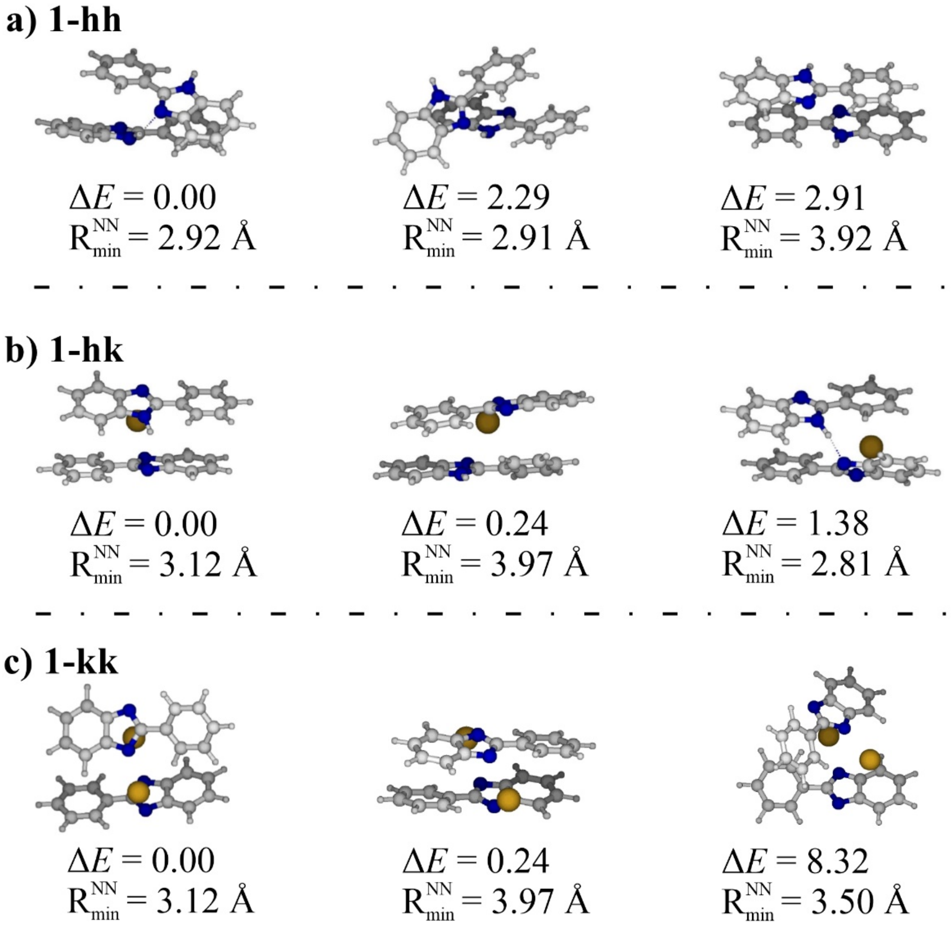

Figure S3: Examples of different types of structures for **1-hh**, **1-hk** and **1-kk** systems. R_{min}^{NN} correspond to value of the shortest N-N distance. ΔE is the relative energy with respect to the corresponding lowest-energy structure (in kcal/mol).

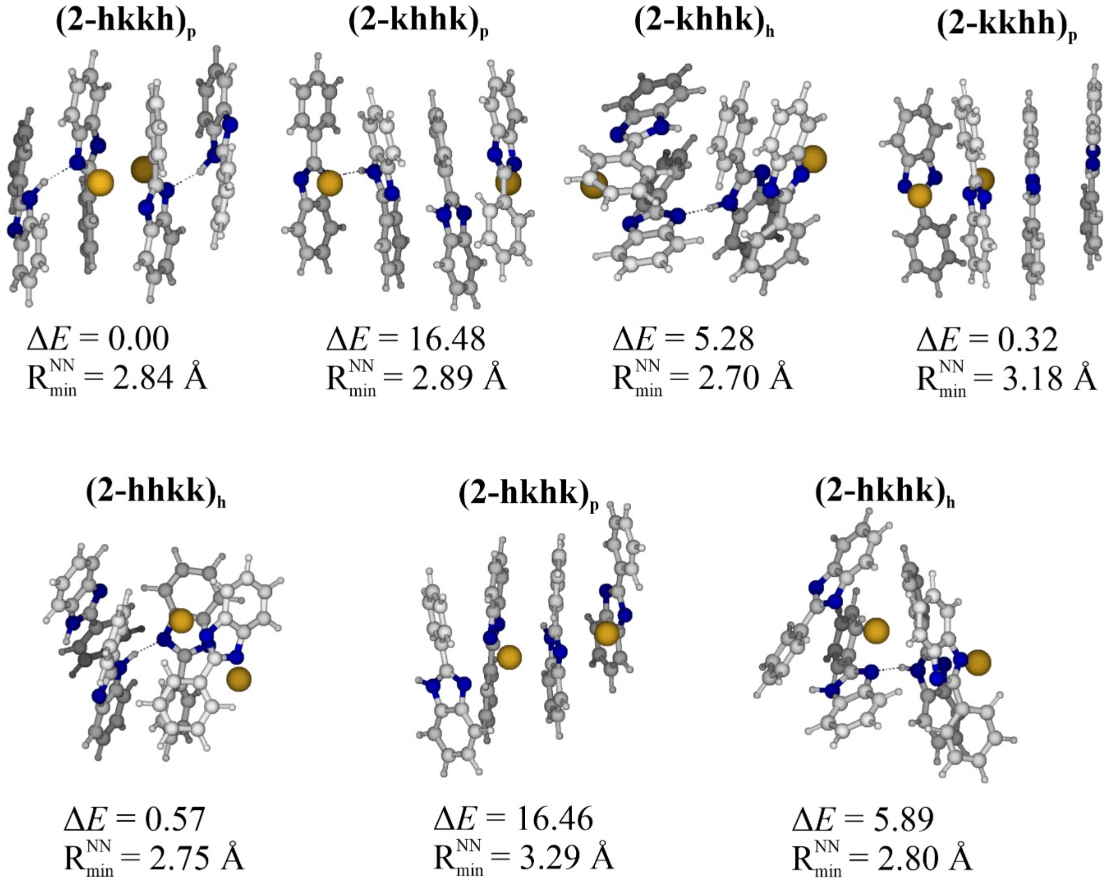

Figure S4: The lowest energy structures for **2** models, for each type of considered group. R_{min}^{NN} correspond to value of the shortest N-N distance. ΔE is the relative energy with respect to the **(2-hkkh)$_p$** structure.

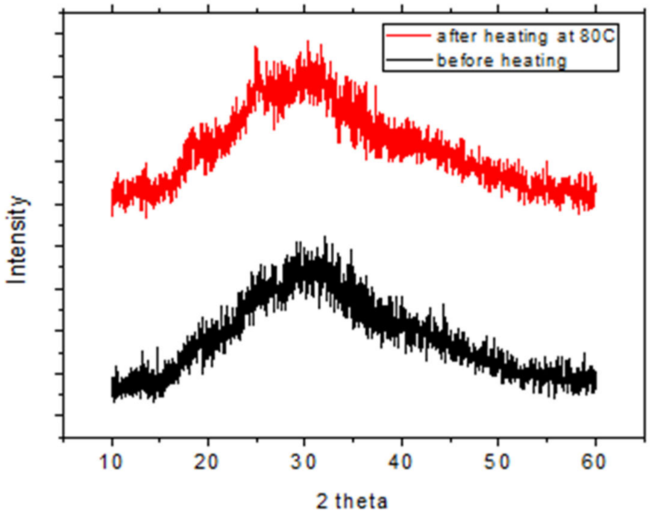

Figure S5: WAXS data of KOH doped gel-state PBI before and after immersion in 25wt% KOH solution at 80°C for 1 day.

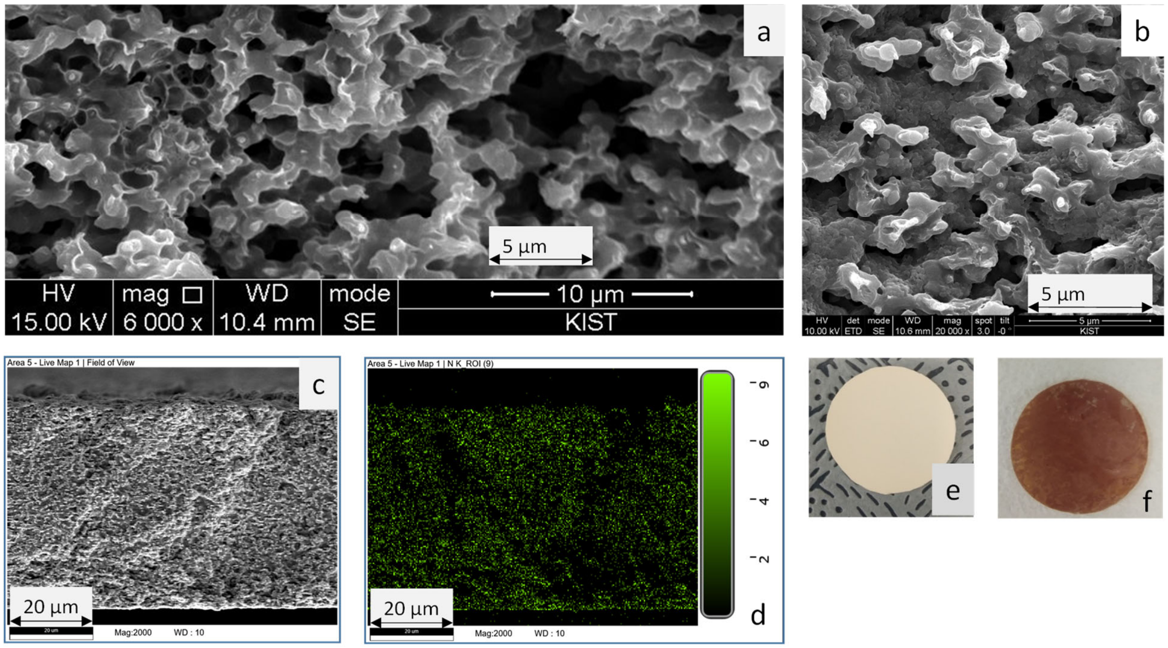

Figure S6: SEM images of PVDF membrane before (a) and after pore filling with PBI (b, c), SEM EDS image showing distribution of nitrogen atoms (d) and photographs of PVDF before (e) and after pore filling with PBI (f).

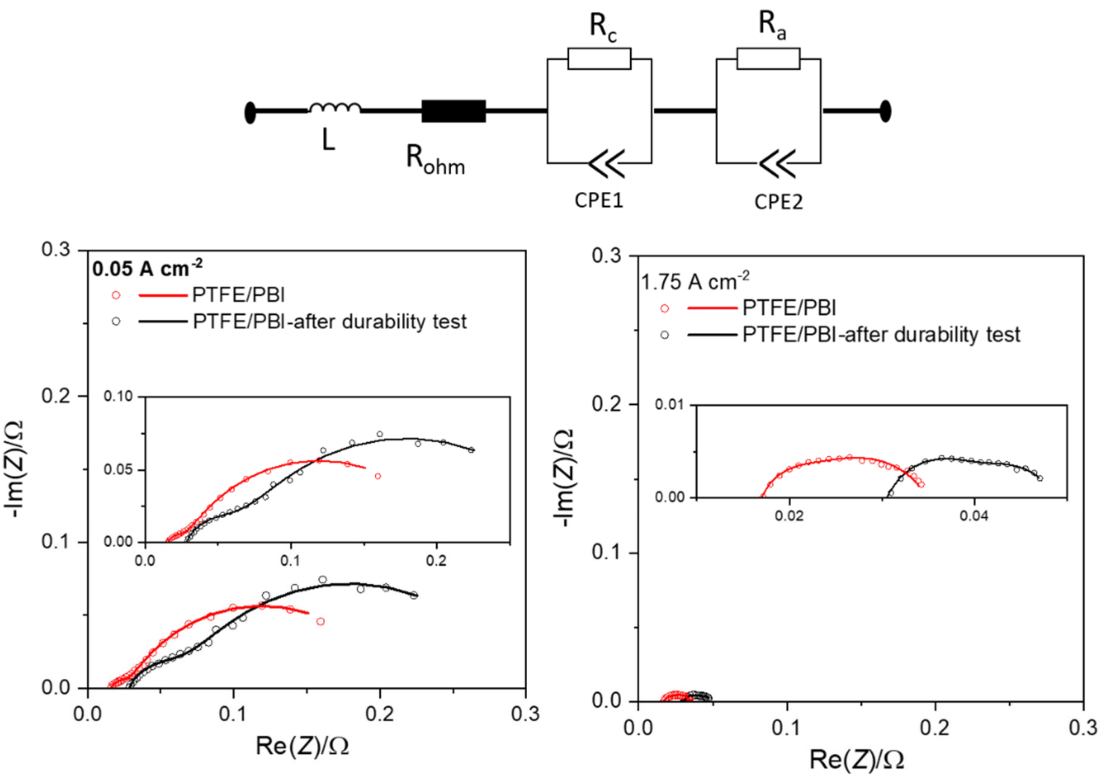

Figure S7: (a) Equivalent circuit used for fitting of Nyquist plots. Nyquist plots from the EIS measurements and their fittings for cell with PTFE/PBI membrane before and after durability at (b) 0.05 A cm^{-2} and (c) 1.75 A cm^{-2}, the magnified Nyquist plots are shown in the inset.

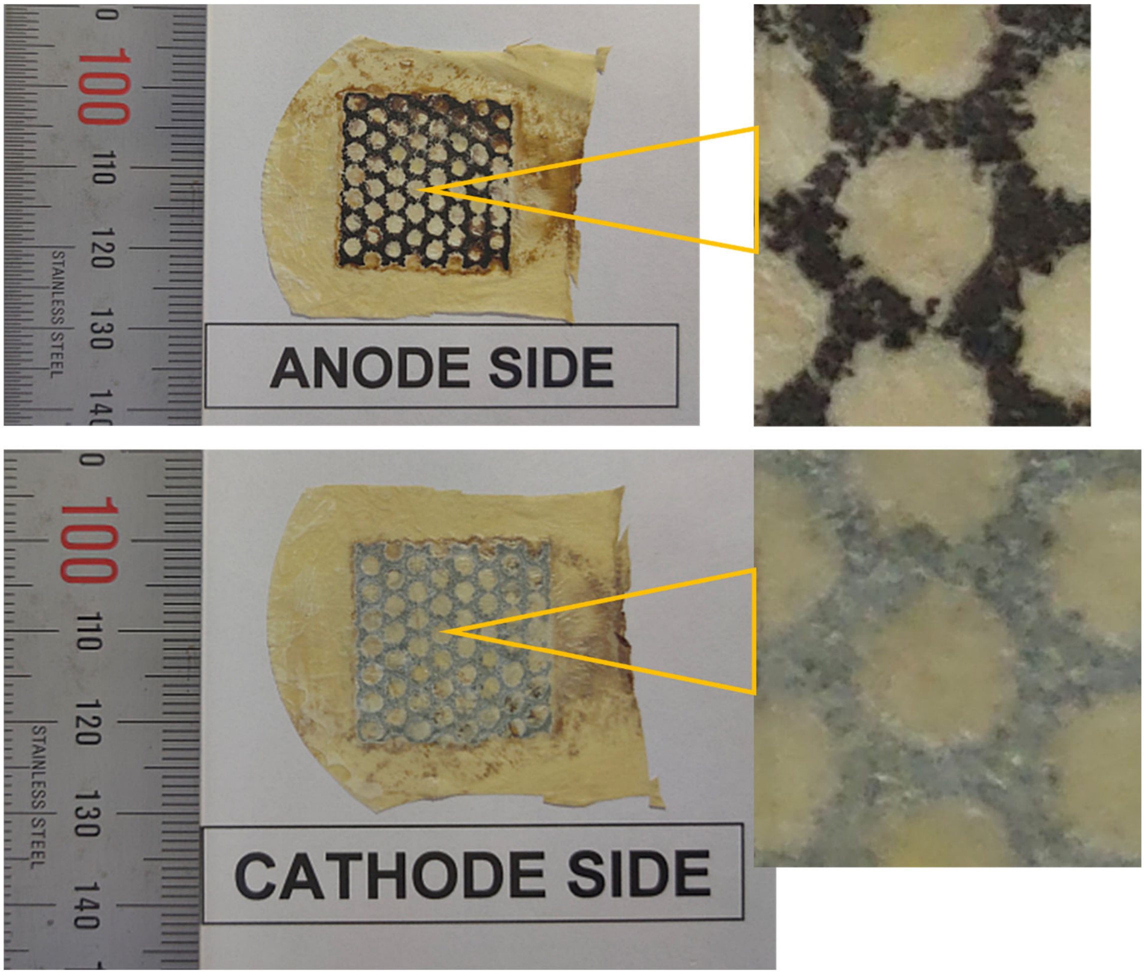

Figure S8: Photographs of a PTFE/PBI membrane after 1000 hours operation in the AEL at 80 °C in 24 wt% KOH feed solution.

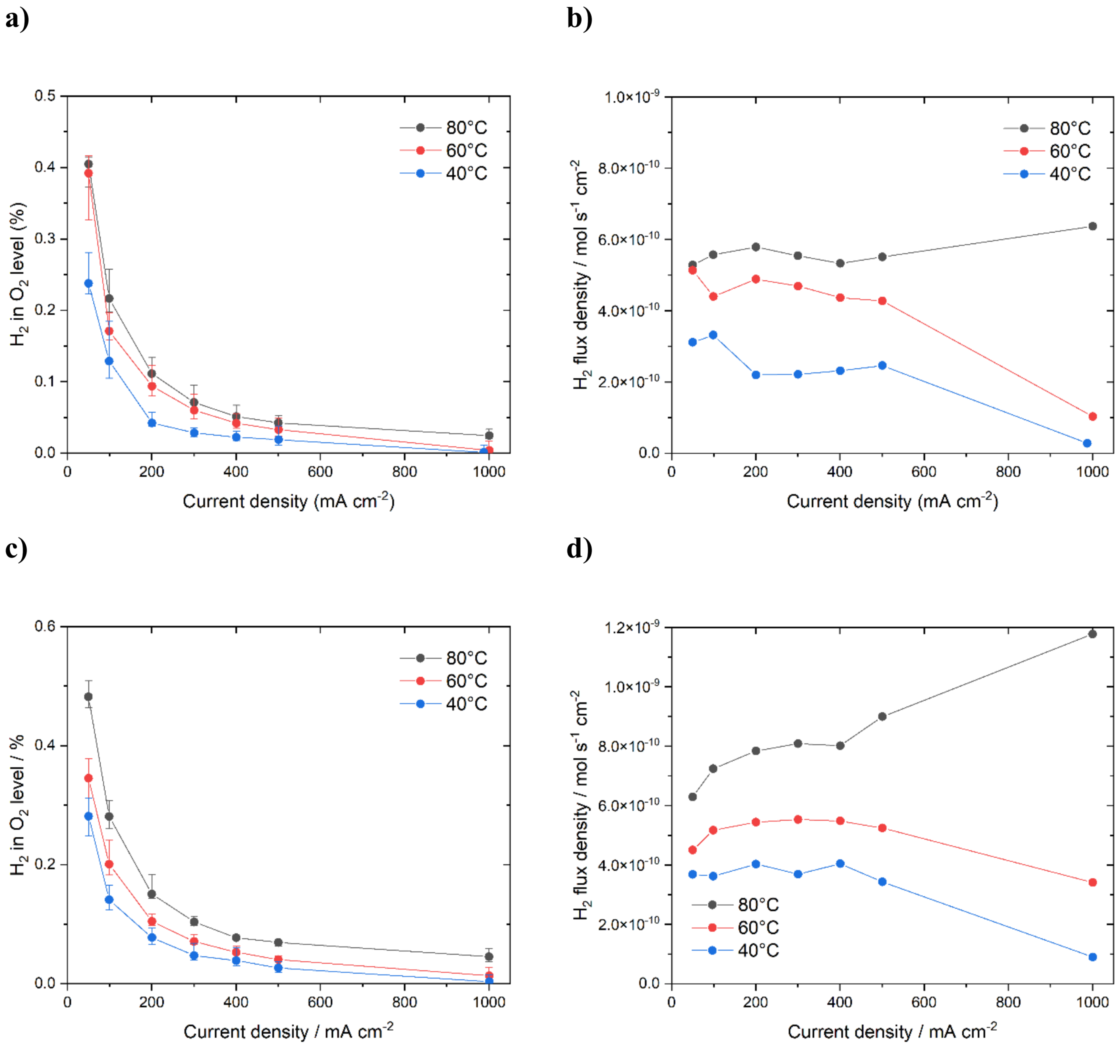

Figure S9: Hydrogen in oxygen levels for Zirfon (a) and PBI (c), as well as hydrogen crossover flux density for Zirfon (b) and PBI (d). Recorded in 24wt% KOH.

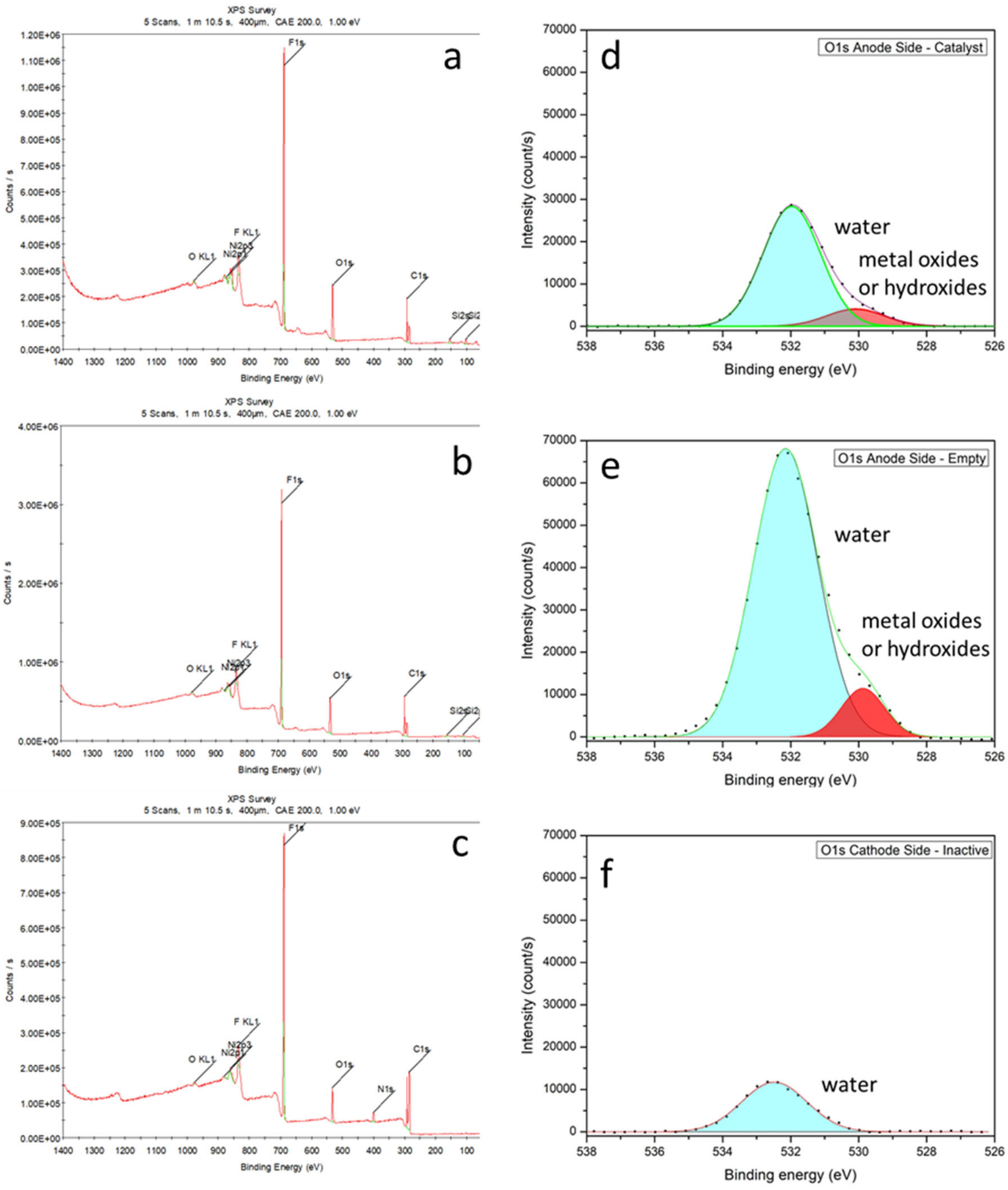

Figure S10: XPS analysis of PTFE/PBI after 1000 hours operation in the electrolyzer. Survey spectra of anode side under the catalyst (a) uncoated active anode area (b) and cathode side inactive area (c); (d, e, f) show the O1s peak. Assignment was made based on data from [S12].

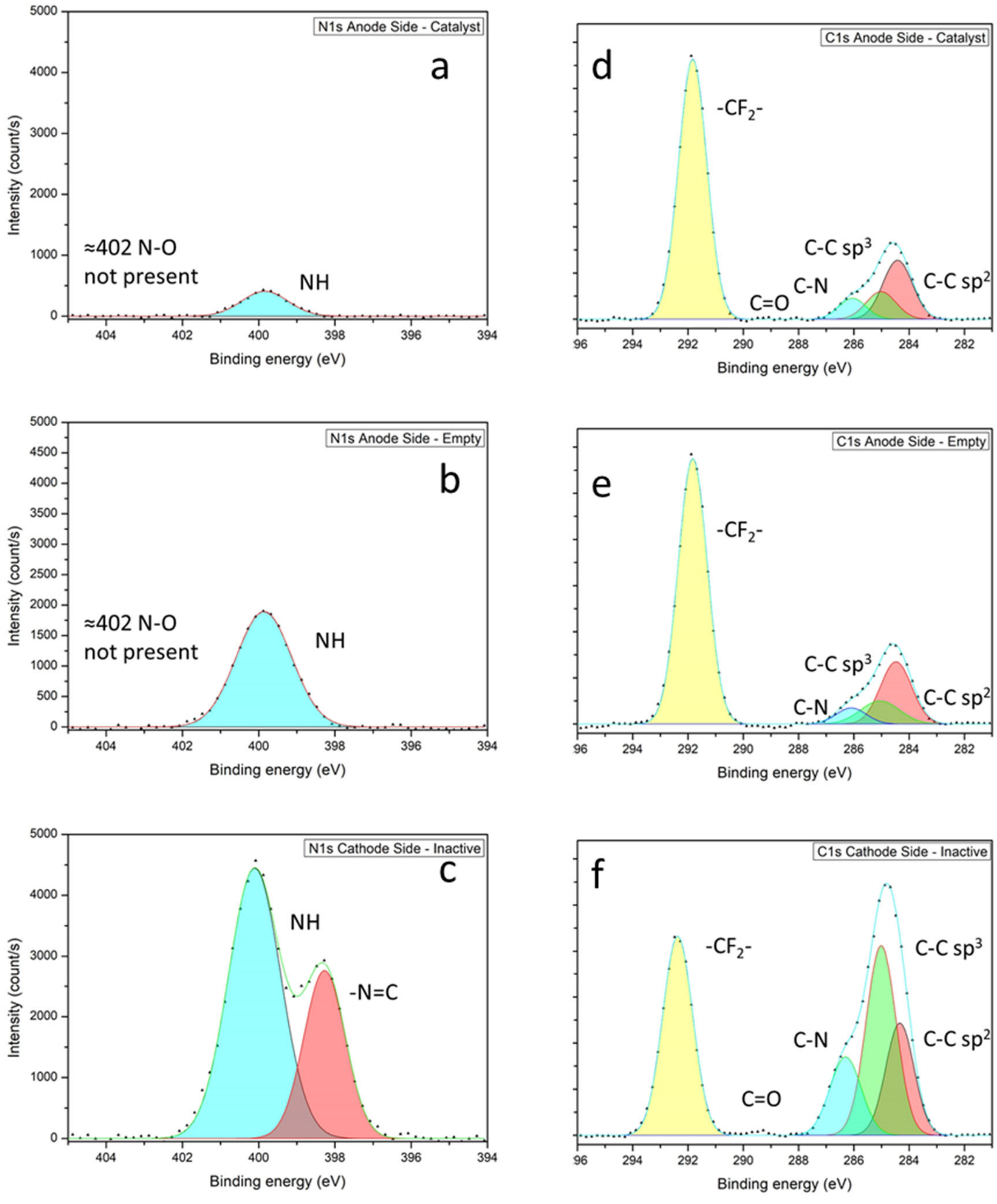

Figure S11: XPS analysis of PTFE/PBI after 1000 hours operation in the electrolyzer. N1s peaks (a,b,c) and C1s peaks (d,e,f).

The survey spectra (**Figure S10**) show that the nitrogen peak is very weak for the anode side samples. This could indicate that PBI was lost on the anode side, or that the coating with PBI was thinner – this cannot be further analysed. The N1s signals for the cathode side show the expected peaks for PBI, an imine peak around 398 eV and a NH peak around 400 eV. For the anode side spectra, the two peaks are merged; this is expected for acid doped PBI: During sample preparation, the catalyst sticking to the membrane was removed by washing with diluted HCl, and the PBI imine groups are expected to be protonated in this process. The most interesting finding for the N1s spectra is that the anode spectra do not show any N-O signals, which should appear around 402 eV [S13]; this suggests that the PBI nitrogen atoms were not oxidized. Similarly, the anode C1s spectra shows those peaks expected for pristine PBI[S13, S14], also in the expected ratio. Different to the literature, which assigns the blue peaks in **Figure S11** to C-O bonds, which do not exist in pristine PBI, we suggest that the blue peaks around 287 are related to protonated C-N groups. Close to the baseline, very weak peaks appear around 288-290. These peaks indicate C=O groups. Because they are also seen on the inactive cathode side, were oxidation is not expected, this could also be the end groups of the polymer chain, i.e. unreacted carboxylic acids, or amide groups for repeat units for which the ring closure from amine-amide to imidazole did not occur.

In conclusion: Although loss of PBI from the anode side cannot be ruled out, based on the higher intensity of PTFE than form PBI, there are no strong indications for chemical degradation of PBI, i.e. no string signals for C=O or N-O groups. This supports that PBI is alkaline stable but may need to be crosslinked to prevent physical changes, partial dissolution or creep.

Table S1: Bubble points of different membranes, wetted with KOH or water. The maximal achievable pressure in the used setup was either 3.0 or 5.6 bar (depending on the status of the gas supply).

	Thickness [µm]	**Bubble point with**	
		KOH [bar]	**Water** [bar]
PBI	185	>3.0	>3.0
Zirfon	500	>5.6	5.6
porous PTFE	65	>3.0	1 bar
porous PVDF	104	2.4	2.5
PVDF/PBI	104	> 5.6	> 5.6
PTFE/PBI	65	>3.0	>3.0

Table S2: Gel Permeation Chromatography of gel-PBI before immersion at 80 °C in 25wt% KOH for 1 week and after. The measurement was done in NMP/LiCl, against polystyrene standards.

	Before testing	**After testing**
Mn	34,127 g/mol	38,452 g/mol
Mw	108,979 g/mol	115,577 g/mol
Polydispersity	3.19	3.01

The molecular weight did not decrease, indicating that the materials is alkaline stable, and that no chain scission occurred. The small increase in the average molecular weights and reduced polydispersity suggest that a small amount of low molecular weight fractions leached out from the membrane during immersion in KOH solution.

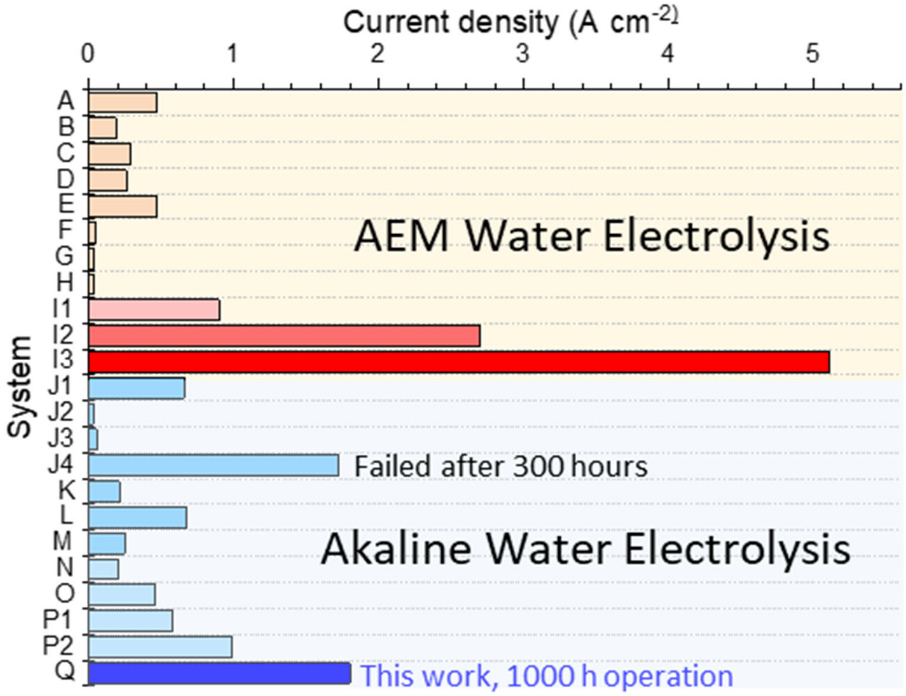

Figure S12: Overview of electrolyser performances of AEMWE and AEL systems found in the literature. The two best performing systems use platinum catalysts, all others are PGM free.

The highest performance was achieved by an AEMWE system using platinum catalysts. The drawbacks of current AEMWE systems are (1) the expected chemical degradation of the AEM's quaternary ammonium groups, (2) the need of an ionomer binder (3) dimensional changes of the ionomer binder, which results in loss of catalyst particles, (4) phenyl oxidation when ionomer binders are in close contact with the platinum catalysts.

In comparison to all AEL systems shown in **Figure S12**, the PTFE/PBI membrane has the highest performance, and did not fail in the single cell test over 1000 hours, whereas the second best performing system (J4) failed after 300 hours.

System	Type	Feed	PGM catalyst	Separator	Note [reference]
A	AEM Water Electrolysis	1M KOH	No	Sustainion	[S15]
B				A201	[S16]
C				A201	[S17]
D				Sustainion	[S18]
E				Fumasep FAS-50	[S19]
F				PBI/mTPN	[S20]
G				SEBS-DABCO	[S21]
H				FAA3-50	[S22]
I1		Water		HTMA-DAPP	[S23]
I2			Yes	HTMA-DAPP	[S23]
I3		1M NaOH		HTMA-DAPP	[S23]
J1	Alkaline Water Electrolysis	> 20wt% KOH	No	Zirfon	Raney nickel[S24]
J2				Zirfon	plain nickel [S24]
J3				mPBI	plain nickel [S24]
J4				mPBI	Raney nickel [S24]
K				160 µm thick unspecified “alkaline membrane” made by ITM Power plc, UK	[S25]
L				polyethersulfone membranes (pore size: 0.1 µm, nominal thickness: 110-150 µm, Sterlitech)	[S26]
M				Zirfon	[S27]
N				Zirfon	[S28]
O				Catalyst coated Zirfon	[S29]
P1				Zirfon	[S30]
P2				300 µm thick Z80	[S30]
Q (this work)				PTFE reinforced gel-PBI	This work

References

[S1] A. Roznowska, K. Dyduch, B. Y. Lee, A. Michalak, Theoretical Study on Preference of Open Polymer vs. Cyclic Products in CO2/Epoxide Copolymerization with Cobalt(III)-Salen Bifunctional Catalysts. J. Mol. Model. 2020, 26 (6), 113. https://doi.org/10.1007/s00894-020-04364-x.

[S2] I. Zadok, H. Long, B. Pivovar, A. Roznowska, A. Michalak, D. R. Dekel, S. Srebnik, Unexpected Hydroxide Ion Structure and Properties at Low Hydration. J. Mol. Liq. 313 (2020) 113485. https://doi.org/10.1016/j.molliq.2020.113485.

[S3] J. J. P. Stewart, Optimization of Parameters for Semiempirical Methods VI: More Modifications to the NDDO Approximations and Re-Optimization of Parameters. J. Mol. Model. 19 (1) (2013) 1–32. https://doi.org/10.1007/s00894-012-1667-x.

[S4] MOPAC2016; Stewart, J.J.P. Stewart Computational Chemistry, Colorado Springs, CO, USA. Available online: http://OpenMOPAC.net (accessed on 2 September 2021)

[S5] G. te Velde, F. M. Bickelhaupt, E. J. Baerends, C. Fonseca Guerra, S. J. A. van Gisbergen, J. G. Snijders, T. Ziegler, Chemistry with ADF. J. Comput. Chem. 22 (9) (2001) 931–967. https://doi.org/10.1002/jcc.1056.

[S6] C. Fonseca Guerra, J. G. Snijders, G. Te Velde, E. J. Baerends, Towards an Order-N DFT Method. Theor. Chem. Acc. (1998). https://doi.org/10.1007/s002140050353.

[S7] ADF. SCM, Theoretical Chemistry, Vrije Universiteit, Amsterdam, The Netherlands. Available online: http://www.scm.com (accessed on 2 September 2021).

[S8] A.D. Becke, Density-fnnctional exchange-energy approximation with correct asymptotic behaviour. Phys. Rev. A 38 (1988) 3098–3100. https://doi.org/10.1103/PhysRevA.38.3098

[S9] J.P. Perdew, Density-functional approximation for the correlation energy of the inhomogeneous electron gas. Phys. Rev. B 33 (1986) 8822–8824. https://doi.org/10.1103/PhysRevB.33.8822.

[S10] S. Grimme, S. Ehrlich, L. Goerigk, Effect of the Damping Function in Dispersion Corrected Density Functional Theory. J. Comput. Chem. 132 (2011) 1456-1465. https://doi.org/10.1002/jcc.21759.

[S11] E. Van Lenthe, E.J. Baerends, Optimized slater-type basis sets for the elements 1-118. J. Comput. Chem. 24 (2003) 1142–1156. https://doi.org/10.1002/jcc.10255.

[S12] A. V. Naumkin, A. Kraut-Vass, S. W. Gaarenstroom, C. J. Powell, NIST X-ray Photoelectron Spectroscopy Database, https://srdata.nist.gov/xps/Default.aspx

[S13] O. Omar, B. Ha, K. Vega, A. Fleischer, H. Moon, J. Shertoka, A. Baileya, M. Mehan, S. K. Gupta, G. A. Takacs, Reaction of ozone with polybenzimidazole (PBI) , Ozone: Sci.Eng. 40 (2018) 392-398. https://doi.org/10.1080/01919512.2018.1446127

[S14] D. Herranz, R. E. Coppola, R. Escudero-Cid, K. Ochoa-Romero, N. B. D'Accorso, J. C. Pérez-Flores, J. Canales-Vázquez, C. Palacio, G. C. Abuin, P. Ocón, Application of Crosslinked Polybenzimidazole-Poly(Vinyl Benzyl Chloride) Anion Exchange Membranes in Direct Ethanol Fuel Cells, Membranes 10 (2020) 349. http://dx.doi.org/10.3390/membranes10110349

[S15] Z. Liu, S. D. Sajjad, Y. Gao, J. Kaczur and R. I. Masel, ECS Trans., 2017, 77, 71–73.

[S16] S. H. Ahn, B.-S. Lee, I. Choi, S. J. Yoo, H.-J. Kim, E. Cho, D. Henkensmeier, S. W. Nam, S.-K. Kim and J. H. Jang, Development of a Membrane Electrode Assembly for Alkaline Water Electrolysis by Direct Electrodeposition of Nickel on Carbon Papers, Appl. Catal. B Environ., 2014, 154–155, 197–205.

[S17] C. C. Pavel, F. Cecconi, C. Emiliani, S. Santiccioli, A. Scaffidi, S. Catanorchi, M. Comotti, Highly Efficient Platinum Group Metal Free Based Membrane-Electrode Assembly for Anion Exchange Membrane Water Electrolysis, Angew. Chem. Int. Ed., 53 (2014), 1378–1381.

[S18] I. V. Pushkareva, A. S. Pushkarev, S. A. Grigoriev, P. Modisha, D. G. Bessarabov, Comparative Study of Anion Exchange Membranes for Low-Cost Water Electrolysis, Int. J. Hydr. Energy. 45 (2020) 26070-26079.

[S19] Z. Liu, S. D. Sajjad, Y. Gao, H. Yang, J. J. Kaczur, R. I. Masel, The Effect of Membrane on an Alkaline Water Electrolyzer, Int. J. Hydr. Energy, 42 (2017) 29661–29665.

[S20] M. Najibah, E. Tsoy, H. Khalid, Y. Chen, Q. Li, C. Bae, J. Hnát, M. Plevová, K. Bouzek, J. H. Jang, H. S. Park, D. Henkensmeier, PBI nanofiber mat-reinforced anion exchange membranes with covalently linked interfaces for use in water electrolysers, J. Membr. Sci., 2021, 640, 119832.

[S21] J. Hnát, M. Plevová, J. Zitka, M. Paidar, K. Bouzek, Anion-selective materials with 1,4-diazabicyclo[2.2.2]octane functional groups for advanced alkaline water electrolysis, Electrochim. Acta, 248 (2017) 547-555.

[S22] E. López-Fernández, J. Gil-Rostra, J. P. Espinós, A. R. González-Elipe, F. Yubero, A. de Lucas-Consuegra, $Cu_xCo_{3-x}O_4$ ultra-thin film as efficient anodic catalysts for anion exchange membrane water electrolysers, J. Power Sources, 415 (2019) 136-144.

[S23] D. Li, E. J. Park, W. Zhu, Q. Shi, Y. Zhou, H. Tian, Y. Lin, A. Serov, B. Zulevi, E. D. Baca, C. Fujimoto, H. T. Chung, Y. S. Kim, Highly quaternized polystyrene ionomers for high performance anion exchange membrane water electrolysers, Nature Energy, 5 (2020) 378-385.

[S24] M. R. Kraglund, M. Carmo, G. Schiller, S. A. Ansar, D. Aili, E. Christensen, J. O. Jensen, Ion-solvating membranes as a new approach towards high rate alkaline electrolyzers, Energy Environm. Sci. 12 (2019) 3313-3318.

[S25] X. Li, F. C. Walsh and D. Pletcher, Nickel based electrocatalysts for oxygen evolution in high current density, alkaline water electrolysers, Phys. Chem. Chem. Phys. 13 (2011) 1162–1167.

[S26] F. Yang, M. J. Kim, M. Brown, B. J. Wiley, Alkaline Water Electrolysis at 25 A cm^{-2} with a Microfibrous Flow-through Electrode, Adv. Energy Mat. 10 (2020) 2001174.

[S27] B. Zayat, D. Mitra, S. R. Narayanan, Inexpensive and Efficient Alkaline Water Electrolyzer with Robust Steel-Based Electrodes, J. Electrochem. Soc. 167 (2020) 114513.

[S28] W.-B. Han, I.-S. Kim, M. J. Kim, W. C. Cho, S.-K. Kim, J. H. Joo, Y.-W. Lee, Y. Cho, H.-S. Cho, C.-H. Kim, Directly sputtered nickel electrodes for alkaline water electrolysis, Electrochim. Acta 386 (2021) 138458.

[S29] C. Karacan, F. P. Lohmann-Richters, M. Shviro, G. P. Keeley, M. Müller, M. Carmo, D. Stolten Fabrication of High Performing and Durable Nickel-Based Catalyst Coated Diaphragms for Alkaline Water Electrolyzers, J. Electrochem. Soc. 169 (2022) 054502.

[S30] H. I. Lee, M. Mehdi, S. K. Kim, H. S. Cho, M. J. Kim, W. C. Cho, Y. W. Rhee, C. H. Kim, Advanced Zirfon-type porous separator for a high-rate alkaline electrolyser operating in a dynamic mode, J. Membr. Sci. 616 (2020) 118541.